# Heterogeneous & Homogeneous & Bio- & Nano-

# CHEM**CAT**CHEM

## CATALYSIS

## Accepted Article

**Title:** Pompon Dahlia-like Cu2O/rGO nanostructures for visible light photocatalytic H2 production and 4-chlorophenol degradation

**Authors:** Sekar Karthikeyan, Kassam Ahmed, Amin Osatiashtiani, Adam Fraser Lee, Karen Wilson, Keiko Sasaki, Ben Coulson, Will Swansborough-Aston, Richard Douthwaite, and Wei Li

This manuscript has been accepted after peer review and appears as an Accepted Article online prior to editing, proofing, and formal publication of the final Version of Record (VoR). This work is currently citable by using the Digital Object Identifier (DOI) given below. The VoR will be published online in Early View as soon as possible and may be different to this Accepted Article as a result of editing. Readers should obtain the VoR from the journal website shown below when it is published to ensure accuracy of information. The authors are responsible for the content of this Accepted Article.

A Journal of

ChemPubSoc
Europe

WILEY-VCH          www.chemcatchem.org

## FULL PAPER

# Pompon Dahlia-like Cu₂O/rGO nanostructures for visible light photocatalytic H₂ production and 4-chlorophenol degradation

Sekar Karthikeyan,*[a],[b] Kassam Ahmed,[a] Amin Osatiashtiani,[a] Adam F. Lee,*[c] Karen Wilson,[c] Keiko Sasaki,[b] Ben Coulson,[d] Will Swansborough-Aston,[d] Richard E. Douthwaite,[d] and Wei Li*[a]

**Abstract:** Hierarchical $Cu_2O$ nanospheres with a Pompon Dahlia-like morphology were prepared by a one-pot synthesis employing electrostatic self-assembly. Nanocomposite analogues were also prepared in the presence of reduced graphene oxide (rGO). Photophysical properties of the hierarchical $Cu_2O$ nanospheres and $Cu_2O$/rGO nanocomposite were determined, and their photocatalytic applications evaluated for photocatalytic 4-chlorophenol (4-CP) degradation and $H_2$ production. Introduction of trace (<1 wt%) rGO improves the apparent quantum efficiency (AQE) at 475 nm of hierarchical $Cu_2O$ for $H_2$ production from 2.23 % to 3.35 %, giving an increase of evolution rate from 234 $\mu mol.g^{-1}.h^{-1}$ to 352 $\mu mol.g^{-1}.h^{-1}$ respectively. The AQE for 4-CP degradation also increases from 52 % to 59 %, with the removal efficiency reaching 95 % of 10 ppm 4-CP within 1 h. Superior performance of the hierarchical $Cu_2O$/rGO nanocomposite is attributable to increased visible light absorption, reflected in a greater photocurrent density. Excellent catalyst photostability for >6 h continuous reaction is observed.

## Introduction

Global energy and health challenges arising from anthropogenic fossil fuel usage (and resulting climate change) and contamination of aquatic environments are driving the development of environmentally benign technologies for energy production/storage and wastewater treatment.[1] Solar energy has emerged as a key resource to address such challenges,[2] both through direct electric power generation, and harnessing by semiconductor photocatalysts for aqueous phase $H_2$ evolution, $CO_2$ reduction and pollutant degradation, and antimicrobial coatings.[3]

Many transition metal oxide semiconductors possess tunable bandgaps and favourable conduction and valence band energies to efficiently separate photoexcited electron($e^-$)-hole($h^+$) pairs.[4] Significant research effort has focused on strategies to tune the photophysical properties of oxide semiconductors by modifying their surface/interface properties through crystal facet engineering, the formation of phase junctions or heterojunctions, and the incorporation of co-catalysts, with the goal of efficient solar light harvesting and improved charge carrier separation/energy matching (and hence high activity and selectivity) to the selected reactant and desired product.[5] Copper (I) oxide is an abundant and low-cost p-type semiconductor with a direct (forbidden) band gap of 2.17 eV and optical band gap of 2.62 eV,[6] which is favourable for overall photocatalytic water splitting to produce $H_2$ under visible light ($\lambda \leq 600$ nm) irradation.[7] $Cu_2O$ has a high optical absorption coefficient, with a high theoretical $H_2$ conversion efficiency of 18 % for water splitting,[8] and power conversion efficiency of 20 %, and hence finds widespread application in photocatalysis environmental pollutant remediation[9] and solar cells.[10] However, the reduction and oxidation potentials of $Cu_2O$ lie within its bandgap resulting in poor photostability,[8] and rapid recombination of photogenerated charge carriers occurs.[11]

Various structural modifications of $Cu_2O$ have been investigated to overcome these limitations, with different morphologies such as nano-wires[12], cubes[13], flowers,[14] and spheres,[15] offering significant improvements in photophysical properties for photocatalytic applications. Size and morphology of $Cu_2O$ nanostructures determine their resulting chemical and physical properties.[16] Hierarchical semiconductors have gained recent interest as they can offer additional control of electronic and optical properties.[17] We reported a hierarchical $Cu_2O$ photocatalyst comprised of individual nanoparticles assembled into porous nanocubes that exhibited a promising hydrogen productivity (water splitting) 15 $\mu mol$ $g^{-1}.h^{-1}$ corresponding to an apparent quantum efficiency (A.Q.E) of 1.2 % in the presence of a Pt co-catalyst.[18] Hierarchical structures also offer improved mass transport to confer higher photocatalytic activity,[19] although existing fabrication routes often employ disposable templates, high temperatures (170 °C),[20] and/or coatings, which increase catalyst production cost and time.[21]

Graphene is a two dimensional monolayer of $sp^2$ hybridised carbon atoms, which due to its unique physical and electronic properties, has attracted global scientific interest and investment since its formal discovery/isolation in 2004.[22] The reduced form of the oxide of graphene, reduced graphene oxide (rGO), exhibits a high surface area, tunable band gap, and excellent electron mobility.[23] rGO surfaces also possess a variety of chemically reactive oxygen functionalities that render it a versatile catalyst support and amenable to mixing with other semiconductors to form hybrid semiconductor composites with potentially superior photocatalytic properties.[24] Indeed, graphite and rGO nanosheets have been explored as supports for dispersing $Cu_2O$

[a]     Dr S. Karthikeyan, K. Ahmed, Dr A. Osatiashtiani, Dr W. Li
        European Bioenergy Research Institute
        Aston University
        Birmingham B4 7ET (UK)
        E-mail: karthik.keyan02@gmail.com; w.li8@aston.ac.uk
[b]     Dr S. Karthikeyan, Prof K. Sasaki
        Department of Earth Resources Engineering
        Kyushu University
        Fukuoka 819-0395 (Japan)
[c]     Prof A.F. Lee, Prof K. Wilson
        RMIT University
        Melbourne VIC3000 (Australia)
        E-mail: adam.lee2@rmit.edu.au
[d]     Dr B. Coulson, W. Swansborough-Aston, Dr R.E. Douthwaite
        Department of Chemistry
        University of York
        York YO10 5DD (UK)

        Supporting information for this article is given via a link at the end of the document.

# FULL PAPER

and TiO$_2$ respectively. Carbonaceous supports are reported to facilitate photoexcited charge separation, and hence improve the photocatalytic activity and photostability of Cu$_2$O,[9a, 25] while thin protective carbon layers arising from glucose carbonisation can significantly increase the photocurrent density and photostability of Cu$_2$O for photoelectrochemical water splitting.[26]

Herein we report the one-pot hydrothermal synthesis and photocatalytic application of hierarchical Cu$_2$O nanospheres and corresponding Cu$_2$O/rGO nanocomposites for 4-chlorophenol (4-CP) degradation and H$_2$ production under visible light. 4-CP was selected as a hazardous, recalcitrant organic compound present in waste water effluent from diverse industrial processes (e.g. pulp and paper, textile and petroleum sectors), and unlike organic dyes does not act as a catalyst photosensitiser. Intermixing rGO and hierarchical Cu$_2$O nanospheres improved photocatalytic activities (and apparent quantum efficiencies) for both reactions relative to the nanospheres alone, without requiring a precious metal co-catalyst or external bias, associated with improved visible light absorption by the nanocomposite. In addition, photodegradation of 4-CP favoured less toxic organic oxidation products

## Results and Discussion

### Structure, photophysical and electronic properties

The synthetic route to Pompon Dahlia-like Cu$_2$O/rGO is illustrated in **Scheme 1**. The Cu(II)-PEG complex was added to graphene oxide to form a hybrid inorganic-organic nanostructure wherein polar groups on the graphene oxide nanosheets promote multivalent bridging (via hydrogen bonding) of GO with ligand coordinated Cu$^{2+}$ ions. Subsequent hydrazine reduction in the presence of NaOH likely promotes a transition from ion-by-ion growth to particle-mediated crystallization of complexed Cu(I)

ions in parallel with reduction of the graphene framework[27] to form a hierarchical Cu$_2$O/rGO nanocomposite. PEG likely acts as a structure-directing agent promoting the formation of discrete Cu$_2$O nanoparticles which coalesce at the rGO surface. Transformation of Cu$_2$O agglomerates into hierarchical structure may proceed by Ostwald ripening and/or self-aggregation and the simultaneous reduction of GO yielding an integrated nanocomposite. A related (albeit template-free) aggregation of hollow Cu$_2$O microstructures via hydrazine reduction is reported in the literature, however neither the photophysical properties nor catalytic performance were described.[28]

The morphologies of hierarchical Cu$_2$O and the Cu$_2$O/rGO nanocomposite were examined by TEM and SEM (**Figure 1** and **2**). TEM of hierarchical Cu$_2$O shows ~400-500 nm aggregates of spherical Cu$_2$O nanoparticles (mean size ~50 nm) in good agreement with SEM images **(Figure S1)**.

Corresponding TEM images of the hierarchical Cu$_2$O/rGO nanocomposite also present semi-transparent graphene oxide sheets that exhibit folds and wrinkles (**Figure 2a-d**) which are in intimate contact with the Cu$_2$O aggregates possibly driven by electrostatic interactions arising from reduction of the parent graphene oxide.[29] Cu$_2$O aggregates and individual particles in the nanocomposite were slightly smaller than those of the free hierarchical Cu$_2$O, being 250-400 nm (**Figure 2a** inset) and 15-30 nm (**Figure 2c** inset) respectively. Aggregates still exhibited a Pompon Dahlia-like morphology (**Figure 2b** inset and **Figure S1**).

Phase analysis by XRD confirmed the exclusive formation of crystalline Cu$_2$O (**Figure 3a**) in the hierarchical Cu$_2$O and Cu$_2$O/rGO nanocomposite, indicated by peaks at 29.56°, 36.41°, 42.31°, 61.36°, and 73.50° associated with characteristic (110), (111), (200), (220), (311), and (222) reflections of pure Cu$_2$O phase (JCPDS 03-0898)[30] and lattice constants a=5.19; b=5.08, c=11.69 and β=90.38. The absence of reduced graphene oxide
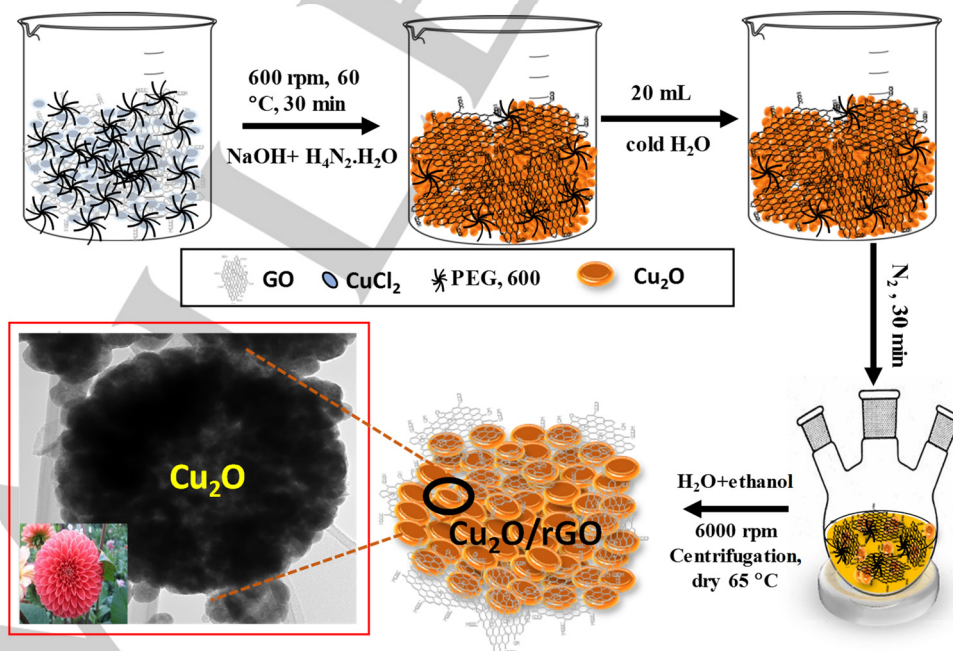


**Scheme 1.** Synthesis of a Pompon Dahlia-like Cu$_2$O/rGO nanocomposite photocatalyst.
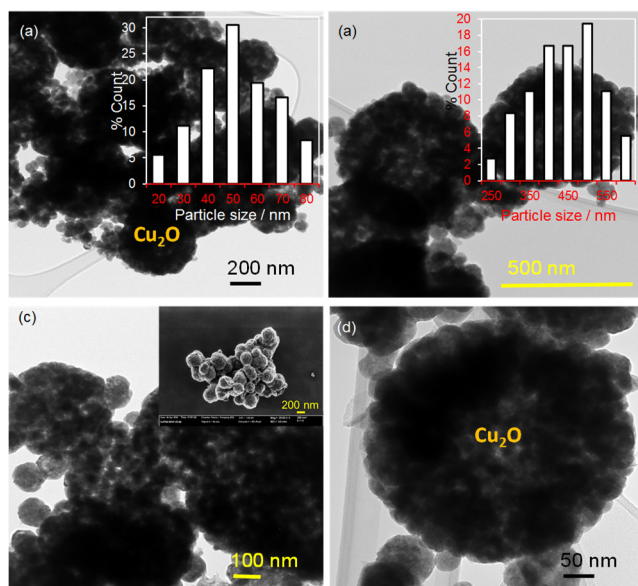
# FULL PAPER



**Figure 1.** (a-d) TEM images of Pompon Dahlia-like hierarchical $Cu_2O$. Insets show particle size distributions (a) for the individual $Cu_2O$ nanoparticles and (b) for the aggregates, and (c) a corresponding SEM image of the aggregates.
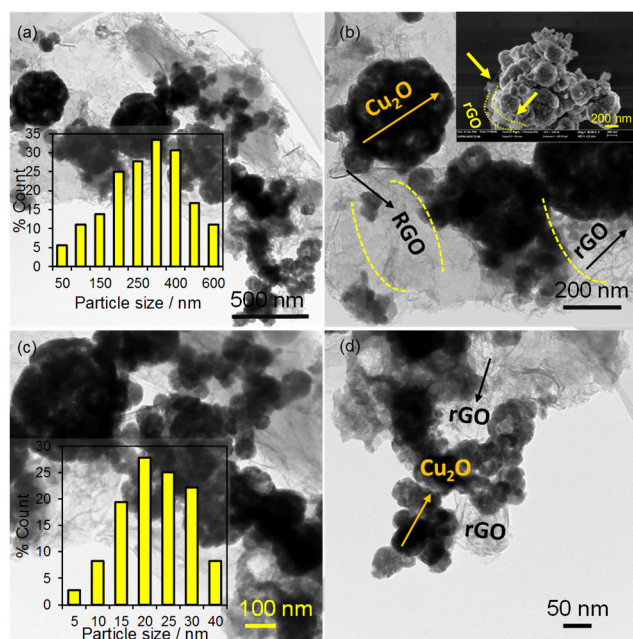


**Figure 2.** (a-d) TEM images of Pompon Dahlia-like hierarchical $Cu_2O/rGO$ nanocomposite. Insets show particle size distributions (a) for the aggregates and (c) for individual $Cu_2O$ nanoparticles, and (b) a corresponding SEM image and (d) high resolution TEM image of the aggregates.

reflections ~25 ° peaks is ascribed to its very low concentration (<0.4 wt%) in the nanocomposite.[31] Volume-averaged crystallite sizes calculated from the Scherrer equation reveal similar (15 nm) $Cu_2O$ nanoparticles for both materials, suggesting the rGO matrix

exerts little impact on the precipitation and reduction of the copper precursor. Textural properties of the hierarchical $Cu_2O$ and $Cu_2O/rGO$ nanocomposite revealed identical, low BET surface areas of 13 $m^2.g^{-1}$ (**Table 1**) comparable to those previously reported for single crystal $Cu_2O$-rGO composites,[32] and identical BJH pore size distributions (**Figure S2**) indicative of ~2 nm mesopores presumably associated with voids between individual $Cu_2O$ nanoparticles in the aggregates. The mesopore volume of the nanocomposite was similar to that of the hierarchical $Cu_2O$. Optical absorption properties of the two materials were studied by DRUVS (**Figure 3b**); although both exhibited broad absorbance between 200-600 nm consistent with literature reports,[32-33] the band edge of the $Cu_2O/rGO$ nanocomposite was red-shifted. Optical band gaps $Eg$ were calculated from the corresponding Tauc plots (**Figure 3c**) using **Eq. 4**:

$$\alpha h v = A(h v - E_g)^n \qquad \qquad \textbf{4}$$

where $A$ is the absorption coefficient and $\alpha$ the linear absorption coefficient determined from the Kubelka-Munk formalism in **Eq. 5**:

$$a = \frac{(1-R)^2}{2R} \qquad \qquad \textbf{5}$$

The resulting direct band gaps were 2.42 eV and 2.13 eV for hierarchical $Cu_2O$ and the $Cu_2O/rGO$ nanocomposite respectively. Since rGO shows weak adsorption >400 nm,[34] the red shift in the nanocomposite must arise from interfacial contact between rGO sheets and $Cu_2O$ and a change in the oxide valence band (VB) and/or conduction band (CB) energies, as previously reported.[35] Such band gap narrowing increase light absorption which could enhance visible light photocatalysis.[32] Note that the $Cu_2O$ band gap is reported to vary between 2.1-2.6 eV, being sensitive to quantum confinement effects and heterojunction formation.[10, 36]

**Table 1.** Photophysical properties of Pompon Dahlia-like hierarchical $Cu_2O$ and $Cu_2O/rGO$ nanocomposite.

| Sample | Crystal size[a] / nm | Particle size[b] / nm | BET area[c] / $m^2.g^{-1}$ | Band gap[d] / eV | CB edge[e] / eV | VB edge[e] / eV |
|---|---|---|---|---|---|---|
| Hierarchical $Cu_2O$ | 15.3 | 400-500 | 13 | 2.42 | -1.12 | +1.3 |
| Hierarchical $Cu_2O/rGO$ | 14.7 | 250-400 | 13 | 2.13 | -1.03 | +1.1 |

[a] XRD. [b] TEM. [c] $N_2$ porosimetry. [d] DRUVS. [e] Calculated from valence band XPS and DRUVS.

The surface copper oxidation state was quantified from high resolution Cu 2p XP spectra (**Figure 4a**), with the hierarchical $Cu_2O$ and $Cu_2O/rGO$ nanocomposite dominated by spin-orbit split doublets with $2p_{3/2}$ binding energies of 932.2 eV and 934.4 eV indicative of $Cu_2O$ and Cu(II) carbonate dihydroxide respectively, and a weak shake-up satellite at 943.4 eV associated with Cu(II) species. The absence of Cu(II) XRD features suggests that $Cu_2(OH)_2CO_3$ arises from the post-synthetic reaction of $Cu_2O$ nanoparticle surfaces with the surrounding atmosphere.[37]
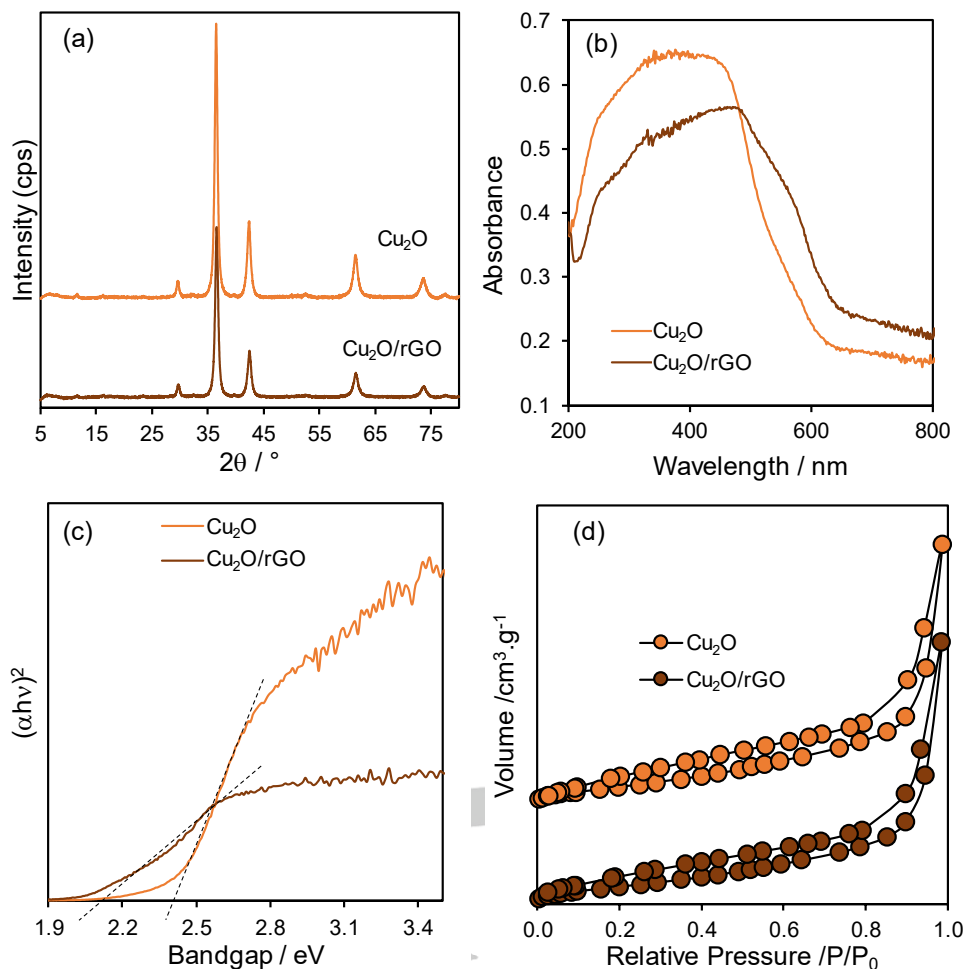
# FULL PAPER



**Figure 3.** (a) XRD patterns, (b) DRUV spectra and (c) corresponding Tauc plots, and (d) $N_2$ adsorption-desorption isotherms of Pompon Dahlia-like hierarchical $Cu_2O$ and $Cu_2O/rGO$ nanocomposite.
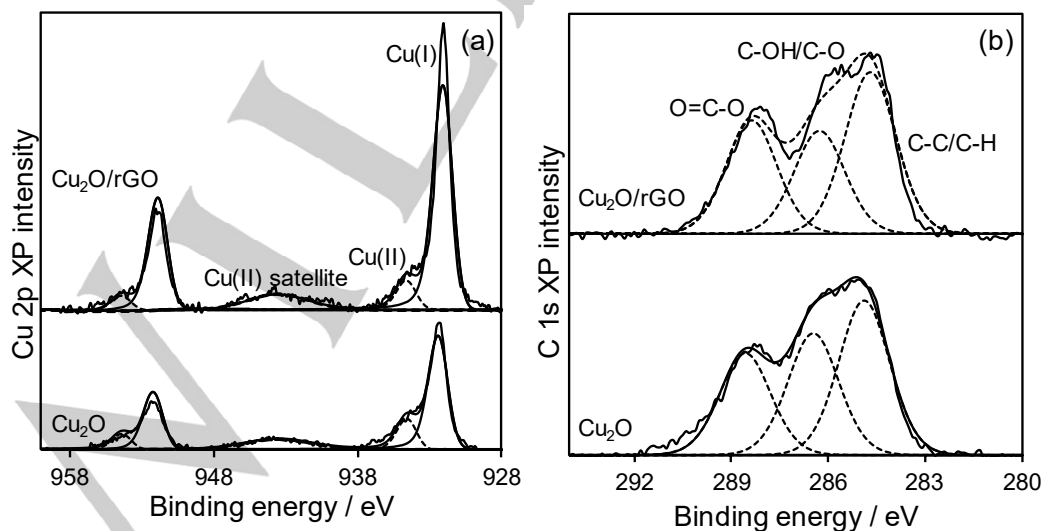


**Figure 4.** (a) Cu 2p and (b) corresponding C 1s XP spectra of Pompon Dahlia-like hierarchical $Cu_2O$ and $Cu_2O/rGO$ nanocomposite.

## FULL PAPER

Spectral fitting reveals that the surfaces of both hierarchical materials predominantly comprise $Cu_2O$ (**Table S1**) with that of the nanocomposite somewhat enriched (88 % versus 79 %). Corresponding C 1s XP spectra revealed almost identical distributions of three distinct chemical environments for both hierarchical materials at 284.6, 286.2, and 288.3 eV **(Figure 4b)**, respectively assigned to the alcohol and ether functions of PEG and surface carbonate.[9a, 38] A small increase in the sp$^2$ carbon environment was observed for the $Cu_2O/rGO$ nanocomposite consistent with graphene incorporation **(Table S2)**.[37] O 1s spectra were consistent with these assignments, exhibiting three distinct chemical environments at 531.4, 533.4, and 535.8 eV arising from $Cu_2O$, carbonate, and PEG ether species **(Figure S3)**, with an enhanced $Cu_2O$ contribution for the nanocomposite consistent with a higher Cu(I):Cu(II) atomic ratio and less surface carbonate.

Charge carrier separation and hence photocatalytic performance depend on the electronic band structure, band alignment and interfacial contact of photocatalysts.[39] Band energies were investigated by valence band XPS (**Figure S4a-c**); the VB potential maxima of hierarchical $Cu_2O$ and the $Cu_2O/rGO$ nanocomposite were +1.30 and +1.10 eV respectively relative to the Fermi level, and corresponding CB minima edges (derived from the optical band gap and valence band XP spectra) were -1.12 eV and -1.03 eV for $Cu_2O/rGO$. The CB minimum is therefore unaffected by formation of the $Cu_2O/rGO$ heterojunction, albeit more negative than previous reports (e.g. -0.42 for oxygen-deficient $Cu_2O$ nanoparticles[40]), and in both cases much greater than required for photocatalytic hydrogen production from water (−0.65 eV at pH 7).[41]

### Photocatalytic $H_2$ production

The photocatalytic activity of the hierarchical $Cu_2O$ and $Cu_2O/rGO$-0.4 wt% nanocomposite for $H_2$ evolution for sacrificial water splitting was assessed under visible light irradiation in the presence of methanol as a sacrificial hole scavenger (**Figure 6a-b**). No evolved oxygen was observed for either catalyst. Hydrogen productivities of 18 $\mu mol.g^{-1}.h^{-1}$ and 31 $\mu mol.g^{-1}.h^{-1}$ were measured for the hierarchical $Cu_2O$ and $Cu_2O/rGO$ nanocomposite respectively, with negligible deactivation during 14 h operation. Increasing the methanol concentration to 10 vol% conferred an almost quantitative increase in $H_2$ productivity, which reached 234 $\mu mol.g^{-1}.h^{-1}$ for the hierarchical $Cu_2O$ and 352 $\mu mol.g^{-1}.h^{-1}$ for the hierarchical $Cu_2O/rGO$ nanocomposite, suggesting that charge carrier recombination is rate-determining for hydrogen evolution over both materials. The greater activity of the nanocomposite equates to an apparent quantum efficiency (AQE) of 3.35 % versus 2.23 % for the hierarchical $Cu_2O$ **(Figure S5)**. Interfacing the $Cu_2O$ semiconductor with rGO nanosheets to form a heterojunction almost doubles the specific activity, consistent with greater visible light absorption.[42] Hydrogen production over the hierarchical $Cu_2O$ was superior to that of non-porous (13 $\mu mol.g^{-1}.h^{-1}$)[43] and $Cu_2O$ nanoparticles (10 $\mu mol.g^{-1}.h^{-1}$)[7] of comparable size, and the AQE. higher than reported for Pt-decorated 500 nm $Cu_2O$ nanocubes (AQE = 1.2 %),[41b] 375 nm hierarchical $Cu_2O$ nanocubes (AQE = 1.2 %),[44] and Pt-free 300-500 nm $Cu_2O$ powder (AQE = 0.3 %)[7] and 150 nm $Cu_2O$

nanostructures on a silicon wafer (AQE in water = 0.3 %) under visible light,[45] demonstrating advantageous photophysical properties of our Pompom Dahlia-like aggregates. Hydrogen production over various $Cu_2O$ photocatalysts is summarised in **Table S3**.
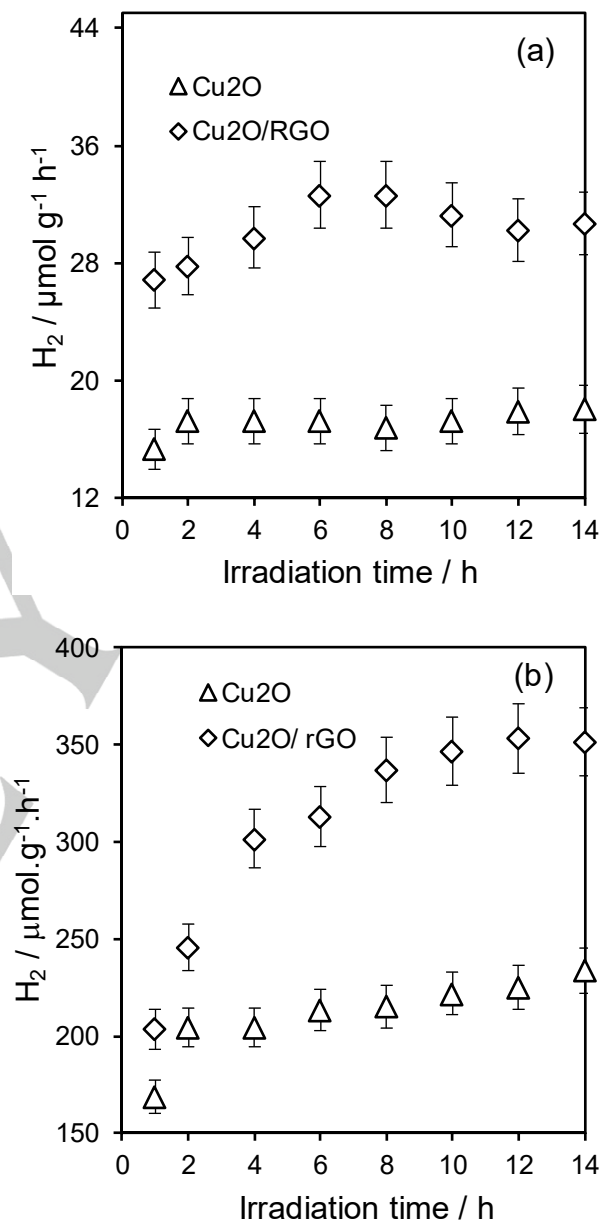
**Figure 5.** Visible light photocatalytic $H_2$ production over Pompon Dahlia-like hierarchical $Cu_2O$ and $Cu_2O/rGO$ nanocomposite with (a) 1 vol% and (b) 10 vol% methanol in water as a sacrificial hole scavenger. Reaction conditions: 0.02 g catalyst, 200 W Hg-Xe ($\lambda$>420 nm).

### Photocatalytic 4-CP removal

Visible light photocatalytic degradation of 4-CP was subsequently studied over the Pompon Dahlia-like hierarchical $Cu_2O$ and $Cu_2O/rGO$ nanocomposite (**Figure S6**). 4-CP was selected as a model recalcitrant organic compound that does not exhibit visible

# FULL PAPER



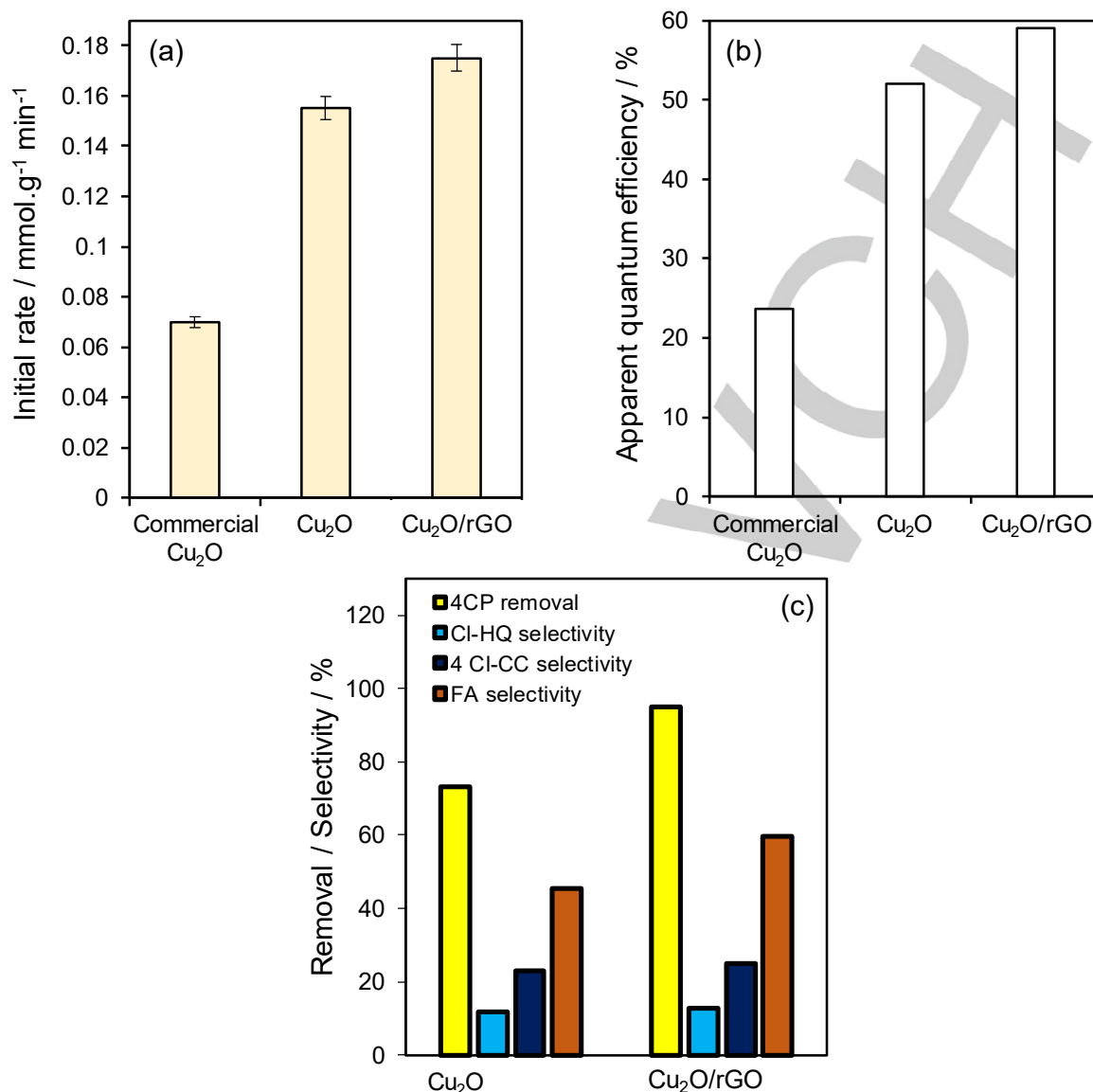**Figure 6.** Visible light photocatalytic 4-CP degradation over Pompon Dahlia-like hierarchical $Cu_2O$ and $Cu_2O/rGO$ nanocomposite and commercial $Cu_2O$ nanoparticles: (a) initial rates of 4-CP removal and (b) corresponding apparent quantum efficiencies after 15 min reaction; and (c) 4-CP removal efficiency and product selectivity after 60 min reaction. Experimental conditions: 0.02 g catalyst, 50 mL of $7.78 \times 10^{-5}$ M aqueous 4-CP, 200 W Hg-Xe arc lamp ($\lambda > 420$ nm).

light absorption and hence cannot act as a photosensitiser which is problematic in mechanistic investigations of photocatalytic dye degradation.[46] Initial rates and AQE for 4-CP removal (**Figure 6a-b**) by the nanocomposite were slightly higher than for the hierarchical $Cu_2O$ aggregates (0.18 versus 0.16 mmol.g$^{-1}$.min$^{-1}$, and 59 versus 52 % respectively). However, the conversion of 4-CP reached 95 % for hierarchical $Cu_2O/rGO$ after 60 min reaction, compared with 73 % for the $Cu_2O$ aggregates alone (and only negligible photolysis in the absence of any catalyst), likely associated with increased light absorption. In comparison to both hierarchical catalysts, commercial $Cu_2O$ nanoparticles exhibited poor activity for 4-CP photocatalytic degradation, achieving only 32 % removal after 60 min, attributed to its low surface area (5

m$^2$.g$^{-1}$ versus 13 m$^2$.g$^{-1}$ for hierarchical $Cu_2O/rGO$). There are no reports of 4-CP photodegradation over $Cu_2O/rGO$ photocatalysts, however the present activity far exceeds other semiconductor photocatalysts (**Table 2**), even those employing UV light and/or high power light sources. The initial rate of 4-CP degradation and 1 h removal efficiency showed a modest dependence on rGO loading, with 0.4 wt% rGO exhibiting the optimal performance, however pure rGO was almost inactive (**Figure S7**).

The major products of 4-CP decomposition were chlorohydroquinone (CL-HQ), 4-chlorocatechol (4Cl-CC), and fumaric acid (FA) (**Figure 6c**). Formation of polyoxygenated intermediates is consistent with a radical mechanism involving photogenerated holes transferred to adsorbed water or surface

# FULL PAPER

hydroxyls to form hydroxyl radicals (•OH), or the reaction of photoexcited electrons with oxygen to produce •OH via $H_2O_2$, although direct oxidation of 4-CP cannot be excluded. The hierarchical $Cu_2O$/rGO favours deeper oxidation and the formation of FA (**Figure 6c**), consistent with more oxidizing equivalents potentially resulting from longer charge carrier lifetimes, and faster charge transfer kinetics (vide infra).[47] Futhermore, $Cu_2O$/rGO exhibited excellent photostability over five consecutive reactions (**Figure S8**).

**Table 2.** Comparison of 4-CP removal efficiency over different photocatalysts.

| Photocatalyst | Experimental details | Rate constant $10^{-2}.min^{-1}$ | Ref. |
|---|---|---|---|
| N-Doped $TiO_2$ | 0.1 g catalyst, 500 W Xe lamp ($\lambda$>420 nm), 100 mL of 10 mg $L^{-1}$ 4-CP, 180 min. | 4.6 | 59 |
| $TiO$/$WO_3$ | 1.2 g/L catalyst, 50 W lamp ($\lambda$>435 nm), $2\times10^{-4}$ M 4-CP, 180 min. | 0.84 | 60 |
| $TiO_2$ – CoPc nanocomposite | 0.1 g catalyst, 128 W Lightex LT50 lamp, 100 mL of 0.013 M 4-CP, 30 min. | 0.042 | 61 |
| Combustion synthesized TiO2 | 1 g/L catalyst, 250 W Xe lamp ($\lambda_{max}$ 470 nm), 0.15 mmol/L 4-CP, 240 min. | 0.049 | 62 |
| Mesoporous g-$C_3N_4$ | 40 mg catalyst, 300 W Xe lamp ($\lambda$>420 nm), $1.2\times10^{-4}$ M 4-CP, 60 min. | 5.26 | 63 |
| Pt/$TiO_2$ | 0.5 g/L catalyst, 11 W Hg lamp ($\lambda$ 200-280 nm), 0.5 mM 4-CP. 120 min. | 0.41 | 64 |
| Heirarchical $Cu_2O$/rGO | 20 mg catalyst, 200 W Hg-Xe arc lamp ($\lambda \geq 420$ nm), 50 mL of $4.2\times10^{-2}$ mM 4-CP, 60 min. | 7.9 | This work |

The chemical state of copper post-reaction was subsequently investigated. XRD and DRUVS revealed negligible change in the phase or electronic properties of the as-prepared hierarchical $Cu_2O$/rGO nanocomposite (**Figure S9**), however XPS evidenced an increase in the proportion of surface Cu(II) species (to 60 %) associated with photo-oxidation of the exterior of $Cu_2O$ nanoparticles.

## Mechanistic studies

Photocatalytic activity for $CO_2$ reduction is also reported to increase following the addition of rGO to $Cu_2O$,[9b] being attributed to increased charge separation across the $Cu_2O$/rGO interface. Charge separation and recombination effects were investigated in water suspensions using steady state photoluminescence and time-resolved photoluminescence (TRPL) which showed very little difference between $Cu_2O$ and $Cu_2O$/rGO (**Figure S10a-b**). It is reported that rGO acts as an electron trap in heterojunction nanocomposites,[48] and photoexcited electrons can transfer from the CB of $Cu_2O$ to rGO, leaving photogenerated holes in the $Cu_2O$ VB.[49] TRPL decay curves **(Figure S10b)** were best fit to a bi-exponential function ( **Eq. 6**).[50]

$$fit = A + A_1 exp^{\frac{(-t)}{(\tau1)}} + A_2 exp^{\frac{(-t)}{(\tau2)}} \qquad \textbf{6}$$

where, A is the baseline correction constant, t is time, $A_1$ and $A_2$ are the contributions of the exponential factors, which include the lifetimes $\tau_1$ and $\tau_2$ of the two excited states. Both lifetimes are short lived consistent with direct radiative emission. The average charge carrier lifetime $\tau$ was determined from **Eq. 7**:

$$\tau = A_1\tau1^2 + A_2\tau2^2/A_1\tau1 + A_2\tau2 \qquad \textbf{7}$$

and shows that photoinduced charge carrier lifetimes are essentially identical for the $Cu_2O$/rGO nanocomposite and hierarchical $Cu_2O$ (**Table 3**). We therefore find no evidence for significant interfacial charge separation across the heterojunction.[51]

**Table 3.** TRPL fitting of Pompon Dahlia-like hierarchical $Cu_2O$ and $Cu_2O$/rGO nanocomposite.

| Photocatalyst | $\tau_1$ / ns | $\tau_2$ / ns | $A_1/(A_1+A_2)$ / % | $A_2/(A_1+A_2)$ / % | $\tau$ / ns | $\chi^2$ |
|---|---|---|---|---|---|---|
| Hierarchical $Cu_2O$ | 1.601 | 2.056 | 23.6 | 76.4 | 1.97 | 1.441 |
| Hierarchical $Cu_2O$/rGO | 1.662 | 2.251 | 23.0 | 77.0 | 2.14 | 1.314 |

Photoelectrochemical measurements showed transient photocurrents (**Figure 7a**) of the $Cu_2O$/rGO composite was approximately double that of the $Cu_2O$ aggregates indicating more redox equivalents are available for photocatalytic reactions. Electrochemical impedance spectroscopy can also provide insight into photoelectrode phenomena. Ideally, an equivalent circuit can be found to model specific photophysical and photoelectrochemical phenomena. More generally, the radius of the impedance curve on a resulting Nyquist plot reflects the resistance in the system. Comparison of data acquired in the dark and under illumination show the reduced radius of the lower frequency feature of the $Cu_2O$/rGO nanocomposite under illumination (**Figure 7b**) indicating that the introduction of rGO facilitates electron migration across the electrode or at the electrode/electrolyte interface.[52] Corresponding Mott Schottky plots under illumination (**Figure 7c**) provide insight into the flat band potential and doping density. Negative slopes were obtained for the hierarchical $Cu_2O$ and $Cu_2O$/rGO nanocomposite, consistent with p-type semiconductors. The x-axis intercept shows the flat band potentials of $Cu_2O$ and $Cu_2O$/rGO nanocomposite are similar at around 1.1 V and 0.98 V, respectively, which compares to 0.55 V reported for a continuous film of cubic $Cu_2O$ nanocrystals.[52] A more positive flat band potential will increase the rate of oxidation of MeOH and water, supporting $H_2$ production and 4-CP degradation, respectively (**Figure 5** and **6**). The slope of the linear portion of the curve in a
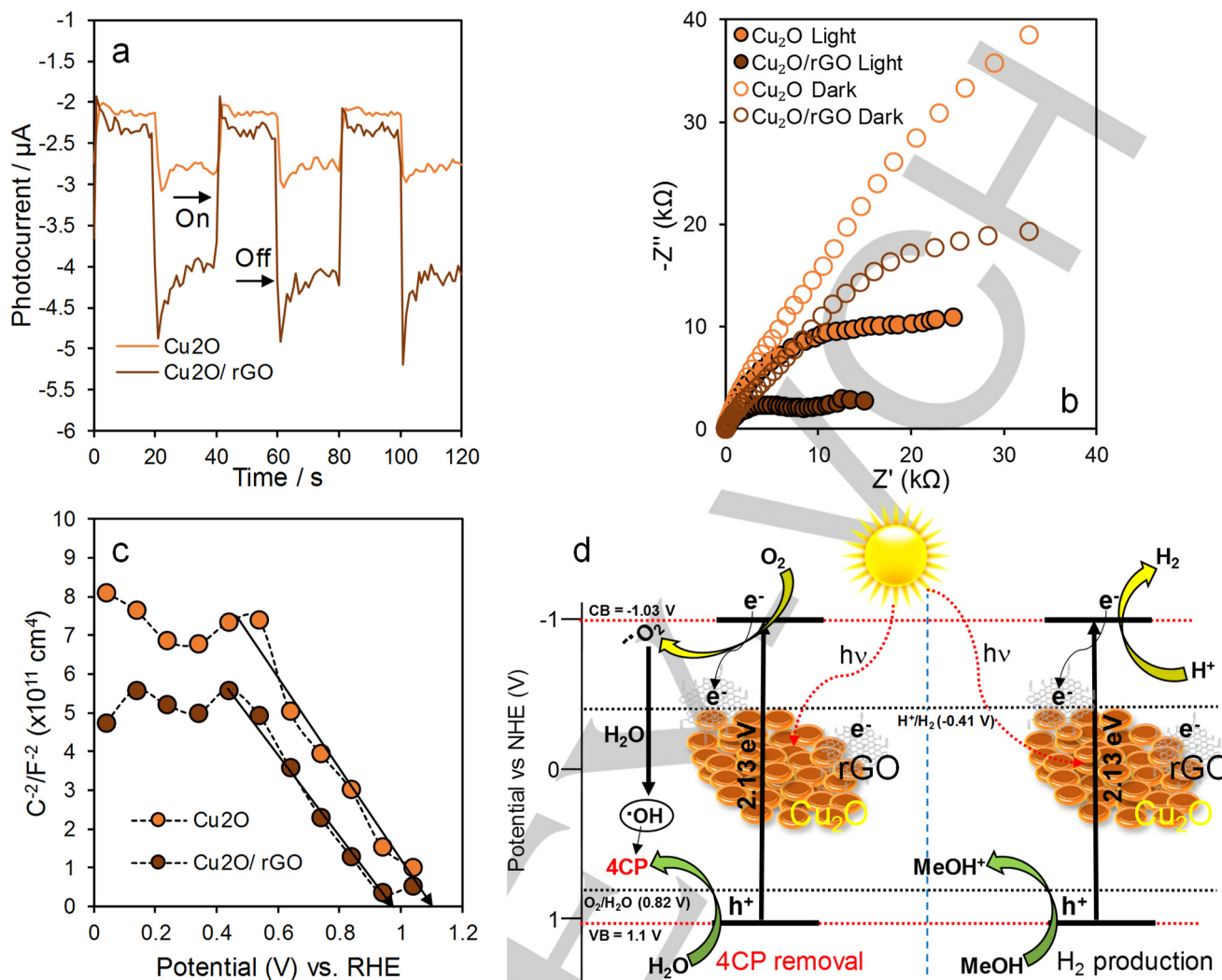
# FULL PAPER



**Figure 7.** (a) Transient photocurrent, (b) EIS (Nyquist) plot at 0 V vs. RHE, (c) Mott-Schottky plot of $Cu_2O$, $Cu_2O/rGO$, and $Cu_2O/rGO$ (200 W Hg-Xe arc lamp and 0.5 M $NaSO_4$ electrolyte), and (d) proposed charge transfer mechanism for $Cu_2O/rGO$.

Mott-Schottky plot is used to calculate the majority carrier density from **Eq. 8**:

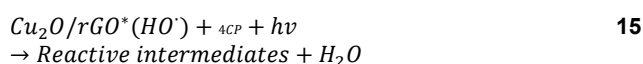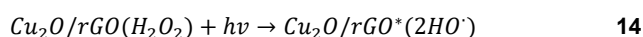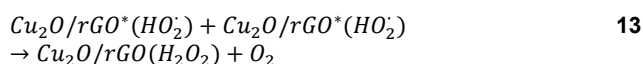$$\frac{1}{C^2} = \frac{2}{\varepsilon\varepsilon_0 e N_A}\left(V - E_{fb} - \frac{k_B T}{e}\right) \qquad 8$$
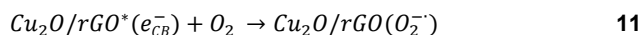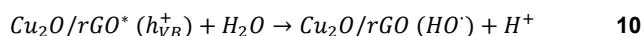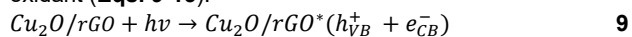
where $\varepsilon$ is the dielectric constant (7.60 for $Cu_2O$[53]), $\varepsilon_0$ is the permittivity of free space, $e$ is the electron charge, $N_A$ is the majority carrier density, $V$ is the applied potential, $E_{fb}$ is the flat band potential, $k_B$ is the Boltzmann's constant and T is the temperature. The majority carrier densities were similar at 1.5 x $10^{19}$ cm$^{-3}$ and 1.7 x $10^{19}$ cm$^{-3}$ for hierarchical $Cu_2O$ and $Cu_2O/rGO$ respectively, both higher that for $Cu_2O$ (3.07 x $10^{17}$ cm$^{-3}$), CuO (2.41 x$10^{18}$ cm$^{-3}$), and $Cu_2O/CuO$ bilayered composite (2.58 x$10^{18}$ cm$^{-3}$) photoanodes prepared by thermal oxidation[52], though less than for electrodeposited/annealed p-type $Cu_2O$-CuO thin films[54] (at 1.3 x$10^{20}$ cm$^{-3}$). Together with the similar flat band potentials, these values suggest there is little difference in either

charge transfer rates or the driving force for charge separation between our two catalysts (in contrast to $Cu_2O/CuO$ bilayered composites[52]). Hence the higher photoactivity of the hierarchical $Cu_2O/rGO$ nanocomposite for hydrogen production and 4-CP degradation compared to hierarchical $Cu_2O$ appears solely associated with its broader absorption of visible light, and not reduced recombination.

A tentative mechanism for photocatalytic 4-CP oxidative degradation over the hierarchical $Cu_2O/rGO$ nanocomposite is illustrated in **Scheme 2**. Under illumination, electrons (e-) within the $Cu_2O$ valence band are photoexcited into the $Cu_2O$ conduction band, and subsequently migrate to rGO sheets. Resulting $Cu_2O$ valence band holes (h+) may then react with hydroxyl ions from the aqueous solution to form •OH radicals, while photoexcited electrons trapped by rGO react with dissolved oxygen to form superoxide $O_2$-• radicals. The latter may further react with water to produce additional •OH through redox

# FULL PAPER

reactions. Reactive intermediates identified by HPLC included chlorohydroquinone (Cl-HQ), chlorocatechol (Cl-CC) and fumaric acid (FA), indicating that the 4-CP photooxidation pathway processes according to **Scheme 2**, with OH• radicals the key oxidant (**Eqs. 9-15**).

$$Cu_2O/rGO + hv \rightarrow Cu_2O/rGO^*(h_{VB}^+ + e_{CB}^-) \qquad \textbf{9}$$

$$Cu_2O/rGO^* (h_{VB}^+) + H_2O \rightarrow Cu_2O/rGO (HO^{\cdot}) + H^+ \qquad \textbf{10}$$

$$Cu_2O/rGO^*(e_{CB}^-) + O_2 \rightarrow Cu_2O/rGO(O_2^{-\cdot}) \qquad \textbf{11}$$

$$Cu_2O/rGO(O_2^{-\cdot}) + H^+ \rightarrow Cu_2O/rGO^*(HO_2^{\cdot}) \qquad \textbf{12}$$

$$Cu_2O/rGO^*(HO_2^{\cdot}) + Cu_2O/rGO^*(HO_2^{\cdot}) \\ \rightarrow Cu_2O/rGO(H_2O_2) + O_2 \qquad \textbf{13}$$

$$Cu_2O/rGO(H_2O_2) + hv \rightarrow Cu_2O/rGO^*(2HO^{\cdot}) \qquad \textbf{14}$$

$$Cu_2O/rGO^*(HO^{\cdot}) + {}_{4CP} + hv \\ \rightarrow Reactive\ intermediates + H_2O \qquad \textbf{15}$$
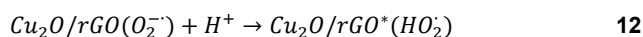


**Scheme 2.** Proposed 4-CP photodegradation pathway.

## Conclusions

A hierarchical Cu$_2$O/rGO nanocomposite was fabricated by electrostatic self-assembly and subsequent low temperature hydrothermal processing. The resulting nanocomposite comprised 300-500 nm aggregates of 15-30 nm Cu$_2$O nanocrystals arranged in a Pompom Dahlia (flower)-like structure, in contact with 1 wt% of rGO nanosheets. This architecture offers broad visible light absorption and excellent stability, resulting in high activity for photocatalytic H$_2$ production from water-alcohol, and 4-CP degradation predominantly to (low toxicity) fumaric acid, without recourse to precious metal co-catalysts. Such hierarchical Cu$_2$O/rGO nanocomposites may provide a low cost approach to solar fuels and chemical (via CO$_2$ reduction) production, and the environmental remediation of recalcitrant wastewater pollutants.

## Experimental Section

*Chemicals*: Copper (II) chloride (CuCl$_2$, 97 %, Aldrich), polyethylene glycol (Alfa Aesar, MW600), sodium hydroxide (NaOH, Sigma), hydrazine monohydrate (H$_4$N$_2$.H$_2$O, Alfa Aesar, 98 %), ethanol (Fisher chemicals, 9.8 %), rGO (Sigma), Cu$_2$O nanoparticles (Sigma, 97 %, 5000 nm particle size, 47 nm crystallite size, 5 m$^2$.g$^{-1}$), 4-chlorophenol (C$_6$H$_5$ClO, Acros organics, 99 %), chlorohydroquinone (Sigma, 85 %) Chlorocatechol (Sigma, 97 %), fumaric acid (Sigma, 99 %), sodium sulfate (Na$_2$SO$_4$, Sigma, 99 %), sodium sulfite (Na$_2$SO$_3$, Sigma, 98 %), potassium bromide (KBr, Sigma, 99 %), Nafion (Sigma), H$_2$O HPLC grade (Sigma), and

acetonitrile HPLC grade (Sigma, 99.93 %) were used without purification. Deionised water was used for all solutions.

*Synthesis of hierarchical Cu$_2$O/rGO*: A Pompon Dahlia (flower)-like Cu$_2$O/rGO catalyst was synthesised by solution phase chemistry under ambient conditions. GO (2 mg) prepared following a literature method[55] was ultrasonicated in 10 mL water for 30 min, to which a mixture of 50 mL of 0.2 M copper chloride and 5 mL of 0.06 M PEG-600 was added and followed by a further 10 min ultrasonication. The resulting mixture was then heated to 60 °C under stirring for 30 min, resulting in a deep blue solution. Subsequently, 8 mL of 2 M NaOH was added into the preceding deep blue solution, and followed by the dropwise addition of 1 M aqueous hydrazine monohydrate (H$_4$N$_2$.H$_2$O) (1 mL in 5 mL of water) under stirring for an additional 5 min. The reaction mixture was then transferred to 20 mL cold water in a multi-neck round-bottomed flask and purged under N$_2$ for 30 min to promote the formation of Cu$_2$O (brownish-yellow colour change). The resulting solid was separated from the reaction mixture by centrifugation at 6000 rpm for 10 min, washed with H$_2$O and then ethanol to remove residual PEG, and finally vacuum dried for 24 h and stored in a vacuum desiccator. Cu$_2$O is formed through the initial complexation of Cu(II) ions with PEG and rGO, and subsequent precipitation as the Cu(I) oxide by hydrazine reduction in the presence of NaOH. Hydroxyl groups from PEG and rGO likely play an important role in controlling the Cu(II) ion density and directing the formation of hierarchical Cu$_2$O structures. The preceding synthesis corresponds to a nominal rGO mass loading of 0.4 % in the hierarchical Cu$_2$O/rGO nanocomposite, and was extended to prepare nanocomposites with nominal rGO mass loadings spanning 2-100 %, and in the absence of GO to prepare pure Dahlia (flower)-like Cu$_2$O with morphologies akin to those reported by Kow et al.[56] In all cases the final catalysts were a reddish-orange colour, produced in ~540 mg yield, and exhibited essentially identical electronic and crystalline properties (**Figure S11**), although high rGO loadings result in encapsulation of Cu$_2$O nanoparticles (**Figure S12**) which may hinder photoexcitation and 4-CP adsorption by the metal oxide.

*Physicochemical characterization*: Crystallinity and phase indexing was performed by powder X-ray diffraction (XRD) using a Bruker-AXS D8 ADVANCE diffractometer operated at 40 kV and 40 mA and Cu K$\alpha$ radiation ($\lambda$=0.15418 nm) between 2$\theta$ 10-80° in 0.02° steps. X-ray photoelectron spectroscopy (XPS) was undertaken on a Kratos Axis HSi spectrometer with monochromated Al K$\alpha$ X-ray source operated at 90 W and normal emission, with magnetic focusing and a charge neutraliser. Spectra were fitted using CasaXPS version 2.3.16, with energy referencing to adventitious carbon at 284.6 eV, and surface compositions derived through applying appropriate instrumental response factors. TEM microscopy was performed on a JEM-2100Plus microscope operated at 200 kV (Warwick University, UK); samples were dispersed in ethanol and ultrasonicated for 5 min and then drop coated on Cu grid coated with carbon film. Brunauer–Emmett-Teller (BET) surface areas were obtained by N2 physisorption at 77 K using a Quantachrome NOVA 4000e porosimeter on samples degassed at 120 °C for 4 h. Surface areas were calculated over the relative pressure range 0.01-0.2, and BJH pore size distributions calculated from the desorption branch of the isotherm for relative pressures >0.35. Diffuse reflectance UV-vis absorption spectra (DRUVS) were recorded on a Thermo Scientific Evo220 spectrometer using an integrating sphere, and KBr as a standard, with band gaps determined between 200-800 nm. Steady state photoluminescence (PL) spectra were measured on a F-4500FL spectrophotometer using 560 nm excitation. Time-resolved photoluminescence (TRPL) spectra were measured on an Edinburgh Photonics FLS 980 spectrometer using pulsed picosecond LED light and 560 nm excitation.

*Photoelectrochemical characterization*: A three electrode photoelectrochemical cell was used, comprising a Pt wire counter

# FULL PAPER

electrode and Hg/Hg$_2$SO$_4$ reference electrode. The photoelectrochemical measurements were converted to the reversible hydrogen electrode (RHE) using **Eq. 1**:

$$E_{V \, vs. \, RHE} = E_{V \, vs. \, \frac{Hg}{Hg_2SO_4}} + E_{\frac{Hg}{Hg_2SO_4}} + 0.059 \, p \qquad \textbf{1}$$

The working electrode was prepared by dropcasting 5 µL of a homogeneous colloidal suspension on a 3 mm diameter glassy carbon electrode. The colloid was prepared by 30 min sonication of a catalyst and Nafion dispersed in a water/ethanol mixture (0.5 mL, 1:1 v/v). Nitrogen degassed 0.5 M Na$_2$SO$_4$ was used as the electrolyte with a pH of 6.8. Irradiation was performed using a 200 W Hg-Xe arc lamp ((Oriel Instruments 66002, λ>420 nm). Nyquist plots were recorded under illumination and in the dark on an Autolab potentiostat with Nova software using a 10 mV AC signal applied between 100 kHz to 0.1 Hz, and Mott-Schottky plots were recorded at 1000 Hz (under illumination and in the dark) using a DC signal spanning -1 to 0 V in 10 mV potential steps.

*Photocatalytic H$_2$ evolution*: Photocatalytic H$_2$ production was performed using hierarchical Cu$_2$O and Cu$_2$O/rGO photocatalysts in a sealed quartz photoreactor (384 mL volume) with a 200 W Hg-Xe arc lamp (Oriel Instruments 66002) and 420 nm cut-off filter to remove UV light; the light intensity inside the reactor was 43.7 mW.cm$^{-2}$. Catalysts (20 mg) were dispersed in 45 mL water with 5mL methanol as a sacrificial hole scavenger and sonicated for 5 min to obtain a uniform distribution. The photoreactor was then purged with He for 1 h in the dark to remove dissolved oxygen, prior to visible light irradiation. Aliquots of gas from the reactor headspace were periodically withdrawn during irradiation using a 1 mL gas syringe and injected into a Shimadzu Tracera GC-2010 Plus gas chromatography fitted with a Carboxen1010 capillary column (30 m×0.53 mm×0.1 µm) and barrier ionization detector (using a He carrier) for gas analysis. Mass-normalised photocatalytic activities are reported to enable quantitative benchmarking of different catalysts, as described in the literature.[57]

*4-CP photocatalytic degradation*: Photocatalytic 4-CP degradation was performed in a sealed quartz photoreactor (260 mL) using a 200 W Hg-Xe arc lamp with 420 nm cut-off filter, and the temperature maintained at 25 °C by a Huber Minichiller. Catalysts (20 mg) were dispersed in 50 mL of 7.78 ×10$^{-5}$ M aqueous 4-CP solution by 7 min ultrasonication in the dark and stirred for a subsequent 120 min in the dark to equilibrate molecular adsorption. Aliquots (1 mL) were periodically withdraw from the reaction mixture for HPLC analysis. Post-reaction catalysts were separated by centrifugation at 8000 rpm for 10 min, and then vacuum dried and stored in a vacuum desiccator for characterisation. The catalyst mass was selected to enable measurement of intrinsic reaction kinetics (**Figure S13**). Concentrations of 4-CP and chlorohydroquinone (Cl-HQ), 4-chlorocatechol (4Cl-CC) and fumaric acid (FA) products were determined from multi-point calibration curves of reference compounds using an Agilent 1260 Infinity Quaternary HPLC equipped with UV diode array and refractive index detectors; an Agilent Zorbax Eclipse plus C18 column was employed at 35 °C using 1 mL/min of a 30 vol% acetonitrile/70 vol% water (HPLC grade) mobile phase, and 280 nm detection. The extent of 4-CP removal, and product selectivity's were calculated from **Eqs. 2 and 3** respectively:

$$\% \, 4CP \, removal = \frac{4CP_{initial} - 4CP_{final}}{4CP_{initial}} \times 100 \qquad \textbf{2}$$

where, the 4CP$_{initial}$ and 4CP$_{final}$ are the mols of 4-CP at the start and end of the irradiation period.

$$\% \, Selectivity = \frac{mols \, Product}{(4CP_{initial} - 4CP_{final})} \times 100 \qquad \textbf{3}$$

[1] R. D. Cortright, R. R. Davda, J. A. Dumesic, *Nature* **2002**, *418*, 964.

[2] Y. Hou, B. L. Abrams, P. C. K. Vesborg, M. E. Björketun, K. Herbst, L. Bech, A. M. Setti, C. D. Damsgaard, T. Pedersen, O. Hansen, J. Rossmeisl, S. Dahl, J. K. Nørskov, I. Chorkendorff, *Nat. Mater.* **2011**, *10*, 434.

[3] a) F. Fresno, R. Portela, S. Suárez, J. M. Coronado, *J. Mat. Chem. A* **2014**, *2*, 2863-2884; b) M. A. Fox, M. T. Dulay, *Chem. Rev.* **1993**, *93*, 341-357.

[4] P. D. Tran, L. H. Wong, J. Barber, J. S. Loo, *Energy Environ. Sci.* **2012**, *5*, 5902-5918.

[5] a) J. Ran, J. Zhang, J. Yu, M. Jaroniec, S. Z. Qiao, *Chem. Soc. Rev.* **2014**, *43*, 7787-7812; b) H. Wang, L. Zhang, Z. Chen, J. Hu, S. Li, Z. Wang, J. Liu, X. Wang, *Chem. Soc. Rev.* **2014**, *43*, 5234-5244.

[6] M. Heinemann, B. Eifert, C. Heiliger, *Phys. Rev. B* **2013**, *87*, 115111.

[7] M. Hara, T. Kondo, M. Komoda, S. Ikeda, J. N. Kondo, K. Domen, M. Hara, K. Shinohara, A. Tanaka, *Chem. Commun.* **1998**, 357-358.

[8] J. Luo, L. Steier, M.-K. Son, M. Schreier, M. T. Mayer, M. Grätzel, *Nano Lett.* **2016**, *16*, 1848-1857.

[9] a) A. Chakravarty, K. Bhowmik, A. Mukherjee, G. De, *Langmuir* **2015**, *31*, 5210-5219; b) X. An, K. Li, J. Tang, *ChemSusChem* **2014**, *7*, 1086-1093; c) R. Chen, S. Pang, H. An, J. Zhu, S. Ye, Y. Gao, F. Fan, C. Li, *Nat. Energy* **2018**, *3*, 655.

[10] A. S. Zoolfakar, R. A. Rani, A. J. Morfa, A. P. O'Mullane, K. Kalantar-Zadeh, *J. Mat. Chem. C* **2014**, *2*, 5247-5270.

[11] S. Sahoo, S. Husale, B. Colwill, T.-M. Lu, S. Nayak, P. M. Ajayan, *ACS Nano* **2009**, *3*, 3935-3944.

[12] W. Z. Wang, G. Wang, X. S. Wang, Y. Zhan, Y. Liu, C. L. Zheng, *Adv. Mater.* **2002**, *14*, 67-69.

[13] W.-C. Huang, L.-M. Lyu, Y.-C. Yang, M. H. Huang, *J. Am. Chem. Soc.* **2011**, *134*, 1261-1267.

[14] S. Jiao, L. Xu, K. Jiang, D. Xu, *Adv. Mater.* **2006**, *18*, 1174-1177.

[15] H. Xu, W. Wang, *Angew. Chem. Int. Ed.* **2007**, *46*, 1489-1492.

[16] S. Karthikeyan, S. Kumar, L. J. Durndell, M. A. Isaacs, C. M. Parlett, B. Coulson, R. E. Douthwaite, Z. Jiang, K. Wilson, A. F. Lee, *ChemCatChem* **2018**, *10*, 3554-3563.

[17] C. M. A. Parlett, K. Wilson, A. F. Lee, *Chem. Soc. Rev.* **2013**, *42*, 3876-3893.

[18] S. Kumar, C. M. Parlett, M. A. Isaacs, D. V. Jowett, R. E. Douthwaite, M. C. Cockett, A. F. Lee, *Appl. Catal. B-Environ.* **2016**, *189*, 226-232.

[19] H. Zhang, Q. Zhu, Y. Zhang, Y. Wang, L. Zhao, B. Yu, *Adv. Funct. Mater.* **2007**, *17*, 2766-2771.

[20] a) L. Chen, Y. Zhang, P. Zhu, F. Zhou, W. Zeng, D. D. Lu, R. Sun, C. Wong, *Sci. Rep.* **2015**, *5*, 9672; b) L. Zhang, P. Ying, B. Yu, L. Wu, J. Wang, X. Gu, S. Chen, R. Zhou, Z. Ni, *RSC Adv.* **2014**, *4*, 42892-42898.

# FULL PAPER

[21] M. Hartmann, *Angew. Chem. Int. Ed.* **2004**, *43*, 5880-5882.

[22] a) K. S. Novoselov, A. K. Geim, S. V. Morozov, D. Jiang, Y. Zhang, S. V. Dubonos, I. V. Grigorieva, A. A. Firsov, *Science* **2004**, *306*, 666-669; b) A. K. Geim, K. S. Novoselov, *Nat. Mater.* **2007**, *6*, 183.

[23] F. Li, L. Zhang, J. Tong, Y. Liu, S. Xu, Y. Cao, S. Cao, *Nano Energy* **2016**, *27*, 320-329.

[24] a) Y. Liang, Y. Li, H. Wang, J. Zhou, J. Wang, T. Regier, H. Dai, *Nat. Mater.* **2011**, *10*, 780; b) Q. Xiang, J. Yu, *J. Phys. Chem. Lett.* **2013**, *4*, 753-759; c) Q. Xiang, B. Cheng, J. Yu, *Angew. Chem. Int. Ed.* **2015**, *54*, 11350-11366.

[25] Z. Gan, X. Wu, M. Meng, X. Zhu, L. Yang, P. K. Chu, *ACS Nano* **2014**, *8*, 9304-9310.

[26] Z. Zhang, R. Dua, L. Zhang, H. Zhu, H. Zhang, P. Wang, *ACS Nano* **2013**, *7*, 1709-1717.

[27] C. K. Chua, M. Pumera, *Chem. Commun.* **2016**, *52*, 72-75.

[28] W. Wang, P. Zhang, L. Peng, W. Xie, G. Zhang, Y. Tu, W. Mai, *CrystEngComm* **2010**, *12*, 700-701.

[29] S. Liu, Z. Chen, N. Zhang, Z.-R. Tang, Y.-J. Xu, *J. Phys. Chem. C* **2013**, *117*, 8251-8261.

[30] S. Sun, X. Zhang, X. Song, S. Liang, L. Wang, Z. Yang, *CrystEngComm* **2012**, *14*, 3545-3553.

[31] a) Q. Li, B. Guo, J. Yu, J. Ran, B. Zhang, H. Yan, J. R. Gong, *J. Am. Chem. Soc.* **2011**, *133*, 10878-10884; b) J. T.-W. Wang, J. M. Ball, E. M. Barea, A. Abate, J. A. Alexander-Webber, J. Huang, M. Saliba, I. Mora-Sero, J. Bisquert, H. J. Snaith, R. J. Nicholas, *Nano Lett.* **2014**, *14*, 724-730.

[32] W. Zou, L. Zhang, L. Liu, X. Wang, J. Sun, S. Wu, Y. Deng, C. Tang, F. Gao, L. Dong, *Appl. Catal. B-Environ.* **2016**, *181*, 495-503.

[33] C. H. Kuo, C. H. Chen, M. H. Huang, *Adv. Funct. Mater.* **2007**, *17*, 3773-3780.

[34] A. Al Nafiey, A. Addad, B. Sieber, G. Chastanet, A. Barras, S. Szunerits, R. Boukherroub, *Chem. Eng. J.* **2017**, *322*, 375-384.

[35] J. Liu, J. Ke, D. Li, H. Sun, P. Liang, X. Duan, W. Tian, M. O. Tadé, S. Liu, S. Wang, *ACS Appl. Mater. Interfaces* **2017**, *9*, 11678-11688.

[36] Y. Chang, J. J. Teo, H. C. Zeng, *Langmuir* **2005**, *21*, 1074-1079.

[37] S. Deng, V. Tjoa, H. M. Fan, H. R. Tan, D. C. Sayle, M. Olivo, S. Mhaisalkar, J. Wei, C. H. Sow, *J. Am. Chem. Soc.* **2012**, *134*, 4905-4917.

[38] L. Xu, F. Zhang, X. Song, Z. Yin, Y. Bu, *J. Mat. Chem. A* **2015**, *3*, 5923-5933.

[39] Y. Xu, A. Li, T. Yao, C. Ma, X. Zhang, J. H. Shah, H. Han, *ChemSusChem* **2017**, *10*, 4277-4305.

[40] M. Singh, D. Jampaiah, A. E. Kandjani, Y. M. Sabri, E. Della Gaspera, P. Reineck, M. Judd, J. Langley, N. Cox, J. van Embden, E. L. H. Mayes, B. C. Gibson, S. K. Bhargava, R. Ramanathan, V. Bansal, *Nanoscale* **2018**, *10*, 6039-6050.

[41] a) G. Nagabhushana, G. Nagaraju, G. Chandrappa, *J. Mat. Chem. A* **2013**, *1*, 388-394; b) S. Karthikeyan, S. Kumar, L. J. Durndell, M. A. Isaacs, C. M. A. Parlett, B. Coulson, R. E. Douthwaite, Z. Jiang, K. Wilson, A. F. Lee, *ChemCatChem* **2018**, *10*, 3554-3563.

[42] D. Mateo, I. Esteve-Adell, J. Albero, A. Primo, H. García, *Appl. Catal. B-Environ.* **2017**, *201*, 582-590.

[43] S. Kakuta, T. Abe, *Electrochem. Solid State Lett.* **2009**, *12*, P1-P3.

[44] S. Kumar, C. M. A. Parlett, M. A. Isaacs, D. V. Jowett, R. E. Douthwaite, M. C. R. Cockett, A. F. Lee, *Appl. Catal. B-Environ.* **2016**, *189*, 226-232.

[45] D. Barreca, P. Fornasiero, A. Gasparotto, V. Gombac, C. Maccato, T. Montini, E. Tondello, *ChemSusChem* **2009**, *2*, 230-233.

[46] N. Barbero, D. Vione, *Environ. Sci. Technol.* **2016**, *50*, 2130-2131.

[47] Y. Li, Z. Sun, S. Zhu, Y. Liao, Z. Chen, D. Zhang, *Carbon* **2015**, *94*, 599-606.

[48] a) G. Katsukis, J. Malig, C. Schulz-Drost, S. Leubner, N. Jux, D. M. Guldi, *ACS Nano* **2012**, *6*, 1915-1924; b) Y. Hou, A. B. Laursen, J. Zhang, G. Zhang, Y. Zhu, X. Wang, S. Dahl, I. Chorkendorff, *Angew. Chem. Int. Ed.* **2013**, *52*, 3621-3625; c) P. N. O. Gillespie, N. Martsinovich, *ACS Appl. Mater. Interfaces* **2019**, *11*, 31909-31922.

[49] Y.-C. Pu, H.-Y. Chou, W.-S. Kuo, K.-H. Wei, Y.-J. Hsu, *Appl. Catal. B-Environ.* **2017**, *204*, 21-32.

[50] a) S. Cao, Q. Huang, B. Zhu, J. Yu, *J. Power Sources* **2017**, *351*, 151-159; b) M. Athanasiou, R. Smith, B. Liu, T. Wang, *Sci. Rep.* **2014**, *4*, 7250.

[51] D. K. Padhi, K. Parida, *J. Mat. Chem. A* **2014**, *2*, 10300-10312.

[52] Y. Yang, D. Xu, Q. Wu, P. Diao, *Sci. Rep.* **2016**, *6*, 35158.

[53] Z. Zhang, P. Wang, *J. Mat. Chem.* **2012**, *22*, 2456-2464.

[54] P. Wang, H. Wu, Y. Tang, R. Amal, Y. H. Ng, *J. Phys. Chem. C* **2015**, *119*, 26275-26282.

[55] W.-K. Jo, S. Kumar, M. A. Isaacs, A. F. Lee, S. Karthikeyan, *Appl. Catal. B-Environ.* **2017**, *201*, 159-168.

[56] J. Kou, A. Saha, C. Bennett-Stamper, R. S. Varma, *Chem. Commun.* **2012**, *48*, 5862-5864.

[57] a) T. Maschmeyer, M. Che, *Angewandte Chemie International Edition* **2010**, *49*, 1536-1539; b) T. Maschmeyer, M. Che, *Angewandte Chemie International Edition* **2010**, *49*, 9590-9591; c) H. Kisch, *Angewandte Chemie International Edition* **2010**, *49*, 9588-9589.

WILEY-VCH

**FULL PAPER**

**Entry for the Table of Contents**

## FULL PAPER

Text for Table of Contents
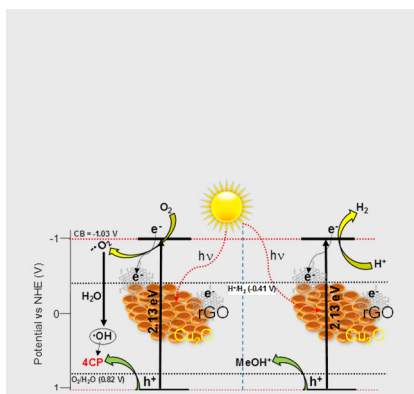


*Author(s), Corresponding Author(s)\**

**Page No. – Page No.**

**Title**